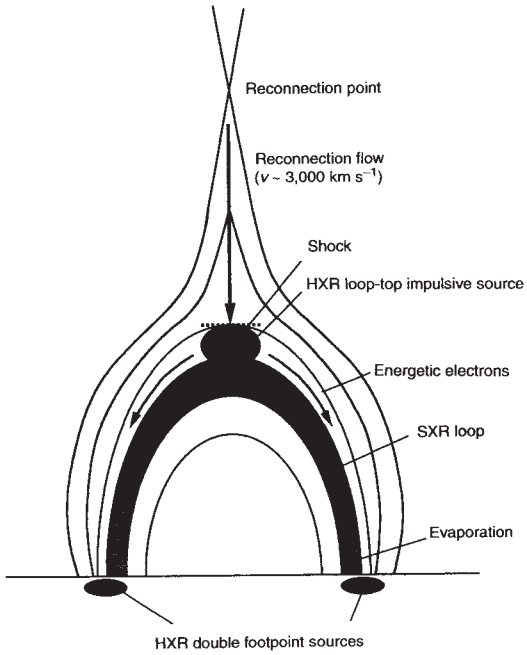

FIG. 3 The magnetic-field geometry for reconnection derived from the present observation. The important features are: elongated antiparallel magnetic fields above an arcade of closed loops; a current sheet (or neutral sheet) formation between them and reconnection of antiparallel magnetic fields. An outflow or jet from the reconnection point impinges on the underlying closed loop and forms a shock, resulting in a high-temperature ($T_e \sim 2 \times 10^8$ K) region just above the closed loop. It is also likely that electrons are accelerated in the shock and stream down along the reconnected field towards the double footpoint sources.

is formed and no strong energization occurs. The soft X-ray flaring loop may represent previously reconnected magnetic fields filled with material evaporated from the dense chromosphere. Perhaps the evaporation is caused not only by energetic electron precipitation but also by heat conduction. In any case, it is a byproduct of the primary energy release.

The observations reported here have revealed for the first time the existence of a loop-top impulsive hard X-ray source in a compact solar flare. There are other examples of this type of source in the Yohkoh data base[22]. We believe that these observations may simplify our theoretical view of solar-flare energy release. The data strongly suggest that we have identified the site of the powerful acceleration of energetic electrons common to solar flares, namely a coronal current sheet. It may now be possible for magnetic reconnection on macroscopic scales to explain compact flares as well as two-ribbon flares. Our discussion of these observations invokes shock formation resulting from the reconnection jet expected in a current-sheet configuration. This discussion was more illustrative than quantitative; it will be instructive to pursue a more thorough analysis of both Yohkoh and ground-based data on this and related flares. □

Received 12 May; accepted 19 August 1994.

1. Pallavicini, R. *Phil. Trans. R. Soc.* A**336,** 389–400 (1991).
2. Carmichael, H. in *AAS-NASA Symp. on the Physics of Solar Flares, NASA SP 50* (ed. Hess, W. N.) 451–456 (NASA, Washington DC, 1964).
3. Sturrock, P. A. *Nature* **211,** 695–697 (1966).
4. Hirayama, T. *Sol. Phys.* **34,** 323–338 (1974).
5. Kopp, R. A. & Pneuman, G. W. *Sol. Phys.* **50,** 85–98 (1976).
6. Hayvaerts, J., Priest, E. R. & Rust, D. M. *Astrophys. J.* **216,** 123–137 (1977).
7. Tsuneta, S. *et al. Publs astr. Soc. Japan* **44,** L63–L69 (1992).
8. Tsuneta, S. in *The Magnetic and Velocity Fields of Solar Active Regions, IAU Colloq. 141* (eds Zirin, H., Ai, G. & Wang, H.) 239–248 (Astr. Soc. Pacific, San Francisco, 1993).
9. Tsuneta, S. in *X-Ray Solar Physics from Yohkoh* (eds Uchica, Y., Watanabe, T., Shibata, K. & Hudson, H. S.) 115–119 (Universal Academy Press, Tokyo, 1994).
10. Tsuneta, S. *et al. Publs astr. Soc. Japan* **44,** L211–L214 (1992).
11. Ogawara, Y. *et al. Sol. Phys.* **136,** 1–16 (1991).
12. Kosugi, T. *et al. Sol. Phys.* **136,** 17–36 (1991).
13. Tsuneta, S. *et al. Sol. Phys.* **136,** 37–67 (1991).
14. Hoyng, P. *et al. Astrophys. J.* **244,** L153–L156 (1981).
15. Duijveman, A., Hoyng, P. & Machado, M. E. *Sol. Phys.* **81,** 137–157 (1982).
16. Sakao, T. thesis, Univ. Tokyo (1994).
17. Hudson, H. S. *et al. Astrophys. J.* **422,** L25–L27 (1994).
18. Hudson, H. S. in *High-Energy Solar Phenomena—A New Era of Spacecraft Measurements AIP Conf. Proc. 294* (eds Ryan, J. M. & Vestrand, W. T.) 151–161 (AIP, New York, 1994).
19. Haisch, B., Strong, K. T. & Rodono, M. *A. Rev. Astr. Astrophys.* **29,** 275–324 (1991).
20. Brown, J. C. *Sol. Phys.* **18,** 489–502 (1971).
21. Hudson, H. S., Canfield, R. C. & Kane, S. R. *Sol. Phys.* **60,** 137–142 (1978).
22. Masuda, S. thesis, Univ. Tokyo (1994).

ACKNOWLEDGEMENTS. We thank H. Hudson for help in polishing the manuscript. The Yohkoh satellite is a Japanese national project, launched and operated by ISAS involving many domestic institutions, with multilateral international collaboration with US and UK.

A photorefractive polymer with high optical gain and diffraction efficiency near 100%

K. Meerholz*, B. L. Volodin*, Sandalphon*, B. Kippelen† & N. Peyghambarian*

* Optical Sciences Center, University of Arizona, Tucson, Arizona 85721, USA
† IPCMS, Groupe d'Optique Nonlinéaire et d'Optoélectronique, Unité Mixte CNRS-ULP-EHICS, Strasbourg, France

PHOTOREFRACTIVE materials are of considerable interest for the development of all-optical devices[1]. The photorefractive effect appears in materials that exhibit an electric-field-dependent refractive index and that are photosensitive, such that the spatial distribution of photogenerated charge carriers is modified on irradiation with light. The diffraction pattern formed by the interference of two coherent light beams within such a material generates a non-uniform internal electric field that in turn modulates the refractive index. The resulting refractive-index pattern forms a grating that can diffract light and thereby give rise to two-beam coupling, whereby one of the writing beams gains energy at the expense of the other—a property that can be exploited in photonic devices. Although the best photorefractive materials currently available are inorganic crystals such as $LiNbO_3$, there is considerable interest in the development of photorefractive polymers[2–8], owing to their structural flexibility, ease of processing and lower cost. We describe here a polymer composite with excellent photorefractive properties. We have achieved a diffraction efficiency approaching 100% and a net two-beam coupling gain of more than 200 cm^{-1}, making these polymeric materials suitable for immediate application in areas such as dynamic holographic storage and optical information processing[1].

In organic materials, the properties required for the photorefractive effect, including photosensitivity, photoconductivity and electro-optic response, are provided by different molecules. As a result, the properties can be optimized separately, unlike in inorganic photorefractive crystals such as $LiNbO_3$. Our investigations were performed on a polymer composite (see Fig. 1) based on the photoconductor poly(*N*-vinylcarbazole) (PVK). Composites using PVK were the first polymers to show efficient photorefractivity[6] and are still among the organic materials with the best performances[4,7]. Photosensitivity in the visible was provided by adding a small amount of 2,4,7-trinitro-9-fluorenone (TNF), which forms a charge-transfer complex with PVK. Crucial for the steady-state performance of a photorefractive composite is the electro-optic chromophore. The latter should possess a large dipole moment μ, a large first hyperpolarizability β, and at the same time a small absorption coefficient α at the operating wavelength. The electro-optic chromophore should be highly soluble in the composite to obtain a strong photorefractive effect. Furthermore, as will be shown below, a large aniso-

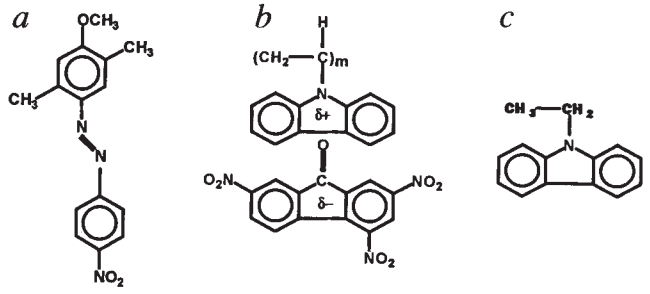

FIG. 1 Chemical structures of the compounds used in the photorefractive composite: *a*, 2,5-dimethyl-4-(*p*-nitrophenylazo)anisole (DMNPAA); *b*, charge-transfer complex of poly(*N*-vinylcarbazole) (PVK) with 2,4,7-trinitro-9-fluorenone (TNF); c, *N*-ethylcarbazole (ECZ).

tropy $\Delta\alpha^*$ of the linear polarizabilities parallel and perpendicular to the molecular axis of this chromophore is beneficial. We chose 2,5-dimethyl-4-(*p*-nitrophenylazo)anisole (DMNPAA), which satisfies these requirements.

To obtain a macroscopic electro-optic effect in the material, the originally randomly oriented electro-optic chromophores have to be aligned by an electric field ('poling'). Besides the alignment of the chromophores, the field also assists the charge photogeneration by reducing the recombination probability and provides the net force for the drift of the carriers. In order to be able to pole the material at room temperature, *N*-ethylcarbazole (ECZ) was added to decrease the glass transition temperature T_g of the material. The composition was DMNPAA:PVK:ECZ:TNF 50:33:16:1 wt%; the concentration of the nonlinear chromophore was significantly higher than in other reported photorefractive polymers (typically $\leqslant$33 wt%)[2-8]. Uniform films of ~105 μm thickness were fabricated by sandwiching the composite between two transparent electrodes, the field thus being applied perpendicular to the sample surface.

Because of the charge separation in photorefractive materials, a phase shift occurs between the original light fringe pattern and the generated index grating. This phase shift is a unique feature of the photorefractive effect, distinguishing it from any other mechanism that gives rise to a light-induced refractive-index modulation. It enables energy transfer between two coherent light beams, the so-called 'two-beam coupling'.

We performed two-beam-coupling experiments to verify the non-local nature of the index gratings, and degenerate four-wave-mixing (DFWM) experiments to test the total grating amplitude. The experimental geometry was identical for both techniques and is shown in Fig. 2 inset. Two coherent 'writing beams' were overlapped in the sample to create a fringe pattern. They were both either 's' or 'p'-polarized (perpendicular or parallel, respectively, to the plane defined by the incoming beam and the sample normal). In order to have a non-zero component of the external field along the grating wave vector **K**, the experiments were performed in a tilted geometry. The grating period was 3.1 μm. In the DFWM experiments, index gratings recorded in the photorefractive material were probed by a weak beam, counterpropagating with the writing beam 1 (Fig. 2 inset) and the intensity of the transmitted and the diffracted light were monitored. In the two-beam-coupling experiments, the counterpropagating beam was absent and the transmission of the two writing beams was measured. All experiments were performed using a single continuous-wave laser diode (9 mW output, wavelengths $\lambda = 675$ nm).

The two-beam-coupling results depend on both the index grating amplitude and its phase shift. As shown in Fig. 2, the steady-state gain coefficient for p-polarized beams Γ_p increases monotonically with the external field E, yielding $\Gamma_p = 220\ \mathrm{cm}^{-1}$ at $E = 90\ \mathrm{V\ \mu m}^{-1}$. The gain by far exceeds the absorption in the sample at this voltage ($\alpha = 13\ \mathrm{cm}^{-1}$), giving a net optical gain of $\Gamma_{p,net} = 207\ \mathrm{cm}^{-1}$. For s-polarized beams, on the other hand, the beam, which gained energy when it was p-polarized, now loses energy for the identical field direction with $\Gamma_s = -40\ \mathrm{cm}^{-1}$ at $90\ \mathrm{V\ \mu m}^{-1}$ (Fig. 2). This is due to opposite signs of the index modulations sensed by the two polarizations.

The DFWM experiments were performed with s-polarized writing beams in order to keep the beam coupling small and to reduce the effects of two-beam energy coupling between the writing beams which causes the grating phase and amplitude to vary throughout the sample[9]. Unlike the gain coefficient Γ, the diffraction efficiency η depends solely on the amplitude of the index grating, not on its phase. Figure 3 shows the DFWM results for p-polarized readout. η_p increases with the electric field and reaches a maximum of 86% at $E = 61\ \mathrm{V\ \mu m}^{-1}$, and the light is completely diffracted. Further increase of the field leads to periodic energy transfer between the diffracted and the transmitted beam; at $E = 81\ \mathrm{V\ \mu m}^{-1}$, all light is again directed into the original probe wave. The sum of diffracted and transmitted signals gradually decreases as the external field increases ($\Delta\alpha = 5\ \mathrm{cm}^{-1}$ at $90\ \mathrm{V\ \mu m}^{-1}$). This is due to electric-field-induced absorption changes in the sample[10] as we verified by an independent transmission measurement in the absence of the writing beams. Similar experiments were performed for s-polarized readout (not shown). The diffraction efficiency is smaller than for p-polarized readout, and no maximum was observed for fields up to $90\ \mathrm{V\ \mu m}^{-1}$.

The dynamics of grating formation are complex. The speed depends on the applied electric field, the light intensity and the

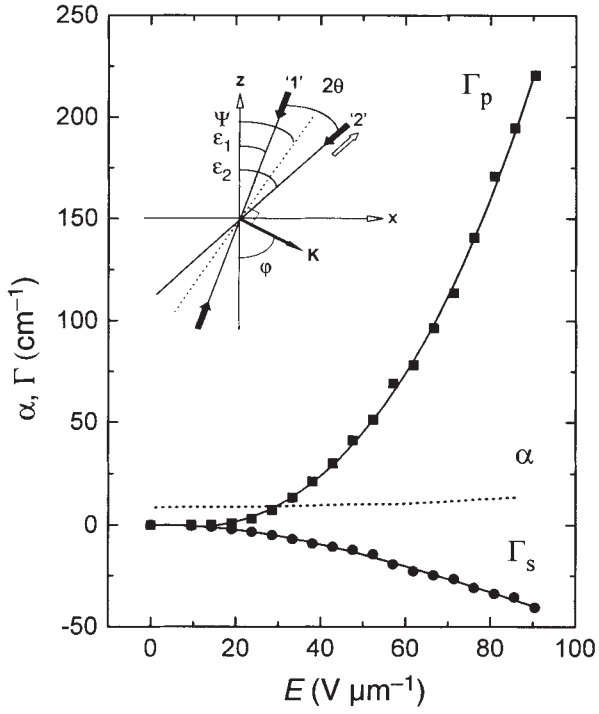

FIG. 2 Two-beam-coupling experiment in DMNPAA:PVK:ECZ:TNF (power density of the pump beam, 1 W cm^{-2}). Main Figure, external-field dependence of the gain coefficient Γ for s- (beam ratio $b = 1.5$; circles) and p-polarized writing beams ($b = 13$; squares). b is the original intensity ratio of the writing beams, defined as $b = (I_2(I_1 = 0))/(I_1(I_2 = 0))$; Γ is calculated from the amplification factor $\gamma = I_1(I_2 \neq 0)/I_1(I_2 = 0)$ measured experimentally using $\Gamma = \{\cos \varepsilon_1 \ln [b\gamma/(b + 1 - \gamma)]\}/d$, where $I_{1,2}$ are the beam intensities of the writing beams, the indices '1' and '2' denote the amplified and the diminished beam, respectively, and ε_1 is the angle of the amplified beam with respect to the sample normal. Also shown is the absorption coefficient α (dashed line). The solid lines are guides to the eye. Inset, write/readout geometry. The angle between the writing beams is $2\theta_{ext} = 22°$ and the tilt angle is $\psi_{ext} = 60°$. Inside the material, $2\theta = 7°$ and $\psi = 29°$; the bulk refractive index was measured (by ellipsometry) as $n = 1.75$.

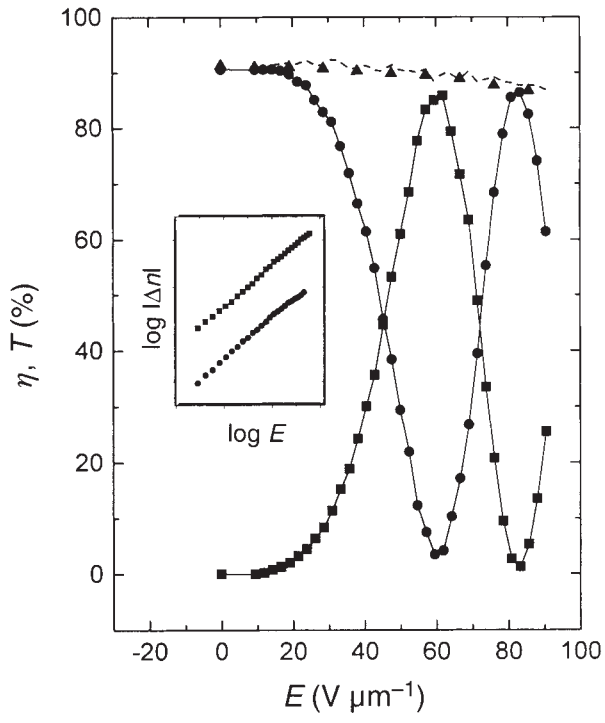

FIG. 3 Degenerate four-wave-mixing experiment in DMNPAA:PVK:ECZ:TNF with s-polarized writing beams (power density, 1 W cm $^{-2}$; beam intensity ratio $b=1.3$) and a p-polarized reading beam (power density, 0.35 mW cm $^{-2}$). Main Figure, external-field dependence of the diffraction efficiency η defined as the intensity ratio of the diffracted probe light and the probe before entering the sample (squares) and the transmission in the presence (circles) and in the absence (triangles), respectively, of the writing beams. The dashed line is the sum of diffracted and transmitted intensity in the presence of the writing beams, indicating that the maximum achievable diffraction efficiency is limited by absorption and reflection losses (~12%). The solid lines are guides to the eye. Inset, log–log plot of the external-field dependence of the index grating amplitudes $|\Delta n_s|$ (circles) and $|\Delta n_p|$ (squares) for s- and p-polarized readout, respectively, obtained from the coupled-waves model for slanted lossy dielectric transmission gratings[11], taking into account the change in absorption with field, but not the small phase and amplitude variations caused by energy exchange between the writing beams.

grating spacing. Under our experimental conditions (see legends of Figs 2 and 3) and at 90 V μm^{-1} the diffraction efficiency rises to ~95% of the maximum value within ~100 ms, reaching a steady-state value after 10 s. The efficiency of the grating drops to 15% of the maximum value within 24 h after all beams and the electric field were switched off. The recorded index pattern can be erased by uniform illumination.

From the DFWM data we calculated the absolute total index grating amplitude in the material $|\Delta n_{s,p}|$ for s- and p-polarized readout, respectively, using Kogelnik's coupled-waves model[11] (see Fig. 3 legend). The observed periodic energy transfer between the transmitted and the diffracted beams in the DFWM experiments is in accordance with this model. The log–log plot of $|\Delta n_{s,p}|$ versus the electric field is shown in Fig. 3 inset. At $E=81$ V μm^{-1} the index grating amplitudes are calculated to be $|\Delta n_s|=1.5\times10^{-3}$ and $|\Delta n_p|=5.5\times10^{-3}$, respectively. The anisotropy ratio $|\Delta n_p/\Delta n_s|=3.7$ is nearly independent of the applied field. Our two-beam-coupling experiments reveal that Δn_s and Δn_p have opposite signs (Fig. 2), that is, $\Delta n_p/\Delta n_s=-3.7$.

To verify that such large field-induced refractive-index changes can be achieved in this material, we carried out ellipsometric measurements in the absence of the writing beams and with the probe polarized at 45° with respect to the vertical axis. Approximately at the fields where the extrema appear in the DFWM experiment we observed that the phase delay between the s- and p-components of the incident light was π and 2π, respectively. The phase delay is given by $\phi=[2\pi d(\Delta n_p-\Delta n_s)]/\lambda\cos\varepsilon_1$ (where d is the sample thickness and ε_1 is defined in Fig. 2), leading to $\Delta n_p-\Delta n_s=5.7\times10^{-3}$ at $E=81$ V μm^{-1}. This is smaller than the value derived from the DFWM experiments for the same field strength ($\Delta n_p-\Delta n_s=7.1\times10^{-3}$) because of the smaller tilt angle ($\varepsilon_{1,ext}=50°$) for the ellipsometry measurements. It is noted that these measurements verify that the space-charge field is smaller than the component of the external field along the grating wave vector ($E_{SC}\leqslant E_{dc}\sin\varepsilon_1$).

The η and Γ values found in our composite material are (by far), the highest reported for organic photorefractive materials to date. They originate from large refractive-index modulations in the material. To find the origin of these excellent properties we further analysed the anisotropy ratio $\Delta n_p/\Delta n_s$. It depends upon the microscopic properties of DMNPAA ($\Delta\alpha^*$, β, μ) and the properties of the host matrix such as its dielectric constant, that is, local field corrections have to be taken into account[11]. For the electro-optic (EO) effect the anisotropy ratio for light polarizations parallel and perpendicular to the local poling-field direction is always positive[13], $(\Delta n_{\parallel}^{EO}/\Delta n_{\perp}^{EO})>0$. The negative sign of $\Delta n_p/\Delta n_s$ thus indicates that effects other than the electro-optic effect play an important role in our material.

Because of the low T_g of the material, the electro-optic chromophores are mobile in the polymer matrix. The samples are poled during the recording by the total electric field E_{tot}, which is the superposition of the uniform external field E_{dc} and the non-uniform internal space-charge field E_{SC} ($E_{tot}=E_{dc}+E_{SC}$), producing a spatially varying orientation of the molecular dipoles in the material. Thus, not only the electro-optic coefficient, but also the linear birefringence of the material is modulated, yielding a stronger photorefractive effect than in materials with a fixed structure such as permanently poled polymers. This phenomenon was discussed recently by Moerner *et al.*[14] as the 'orientational enhancement' mechanism. The anisotropy ratio for the electric-field-induced birefringence (BR) is always negative[13], $(\Delta n^{BR}/\Delta n_{\perp}^{BR})<0$. Assuming that the total index change is the sum of the individual changes by the birefringence and the electro-optic effect, the negative sign of $\Delta n_p/\Delta n_s$ unambiguously shows that the contribution of birefringence to the total index modulation is significant.

Our results offer a significant advance in the new field of research on photorefractive polymers. The excellent performance of the composite DMNPAA:PVK:ECZ:TNF can be explained by the high chromophore content, and by its low T_g, allowing the periodic orientation of the chromophores by the non-uniform internal field. This leads to refractive index gratings due to the birefringence and the electro-optic effect, and therefore to an enhanced photorefractive effect. The results provide evidence that the birefringence is mostly responsible for the excellent photorefractive properties of our material. Contributions from higher-order phenomena cannot be completely excluded. Diffraction from absorption gratings can be safely neglected because the maximum field-induced absorption change of 5 cm^{-1} gives an estimated diffraction efficiency of $\eta\approx(\Delta\alpha d/4)^2\approx1.5\times10^{-4}$. The improved quality of the films allows the application of high electric fields, enabling the observation of complete diffraction and large optical gain using a low-power laser diode. □

Received 25 April; accepted 24 August 1994.

1. Günter, P. & Huignard, J. P. *Photorefractive Materials and Their Applications* Vols 1 & 2 (Springer, Berlin, 1988 & 1989).
2. Ducharme, S., Scott, J. C., Twieg, R. J. & Moerner, W. E. *Phys. Rev. Lett.* **66,** 1846–1849 (1991).
3. Tamura, K., Padias, A. B., Hall, H. K. Jr & Peyghambarian, N. *Appl. Phys. Lett.* **60,** 1803–1805 (1992).
4. Cui, Y., Zhang, Y., Prasad, P. N., Schildkraut, J. S. & Williams, D. J. *Appl. Phys. Lett.* **61,** 2132–2134 (1992).

5. Kippelen, B., Tamura, K., Peyghambarian, N., Padias, A. B. & Hall, H. K. Jr *Phys. Rev.* B**48,** 10710–10717 (1992).
6. Donkers, M. C. J. M. *et al. Opt. Lett.* **18,** 1044–1046 (1993).
7. Kippelen, B. *et al. Electron. Lett.* **29,** 1873–1874 (1993).
8. Liphard, M. *et al. Science* **263,** 367–369 (1994).
9. Kukhtarev, N. V., Markov, V. B., Odulov, S. G., Soskin, M. S. & Vinetskii, V. L. *Ferroelectrics* **22,** 949–960 (1979).
10. Weiser, G. *Phys. Status Solidi* A**18,** 347–359 (1973).
11. Kogelnik, H. *Bell System Tech. J.* **48,** 2909–2947 (1969).
12. Singer, K. D., Kuzyk, M. G. & Sohn, J. E. *J. Opt. Soc. Am.* B**4,** 968–976 (1987).
13. Wu, J. W. *J. Opt. Soc. Am.* B**8,** 142–152 (1991).
14. Moerner, W. E., Silence, S. M., Hache, F. & Bjorklund, G. C. *J. Opt. Soc. Am.* B**11,** 320–330 (1994).

ACKNOWLEDGEMENTS. This work was supported by the USAF Office of Scientific Research and by the US National Science Foundation. K.M. thanks the Deutsche Forschungsgemeinschaft for a postdoctoral fellowship.

Transient nature of CO_2 fertilization in Arctic tundra

Walter C. Oechel*, Sid Cowles†, Nancy Grulke‡, Steven J. Hastings*, Bill Lawrence§, Tom Prudhomme‖, George Riechers¶, Boyd Strain#, David Tissue# & George Vourlitis*

* Global Change Research Group, and Systems Ecology Research Group, San Diego State University, San Diego, California 92182, USA
† Stanford Human Genome Center, Department of Genetics, Stanford University, Stanford, California 94305–5120, USA
‡ Forestry Science Laboratory, 3200 Southwest Jefferson Way, Corvallis, Oregon 97331, USA
§ NASA, Goddard Space Flight Center, Code 923, Biospheric Sciences, Greenbelt, Maryland 20771, USA
‖ Omega Medical Systems, Inc., PO Box 18708, Raleigh, North Carolina 27619, USA
¶ Statewide Air Pollution Research Center, University of California, Riverside, California 92521, USA
# Botany Department, Duke University, Durham, North Carolina 27706, USA

THERE has been much debate about the effect of increased atmospheric CO_2 concentrations on plant net primary production[1,3] and on net ecosystem CO_2 flux[3–10]. Apparently conflicting experimental findings could be the result of differences in genetic potential[11–15] and resource availability[16–20], different experimental conditions[21–24] and the fact that many studies have focused on individual components of the system[2,21,25–27] rather than the whole ecosystem. Here we present results of an *in situ* experiment on the response of an intact native ecosystem to elevated CO_2. An undisturbed patch of tussock tundra at Toolik Lake, Alaska, was enclosed in greenhouses in which the CO_2 level, moisture and temperature could be controlled[28], and was subjected to ambient (340 p.p.m.) and elevated (680 p.p.m.) levels of CO_2 and temperature (+4 °C). Air humidity, precipitation and soil water table were maintained at ambient control levels. For a doubled CO_2 level alone, complete homeostasis of the CO_2 flux was re-established within three years, whereas the regions exposed to a combination of higher temperatures and doubled CO_2 showed persistent fertilization effect on net ecosystem carbon sequestration over this time. This difference may be due to enhanced sink activity from the direct effects of higher temperatures on growth[16,29–33] and to indirect effects from enhanced nutrient supply caused by increased mineralization[10,11,19,27,34]. These results indicate that the responses of native ecosystems to elevated CO_2 may not always be positive, and are unlikely to be straightforward. Clearly, CO_2 fertilization effects must always be considered in the context of genetic limitation, resource availability and other such factors.

Net ecosystem carbon balance is the difference between gross primary productivity and losses from plant and soil respiration (together with generally small losses to herbivores). In the historical and recent geological past (Holocene epoch), net primary productivity of permafrost-dominated northern ecosystems often exceeded heterotrophic respiration due to the cold, wet soil environment[34,35]. As a result, these ecosystems during the Holocene were net sinks for carbon with respect to the atmosphere of up to ~0.1 to 0.3 petagrams of carbon per year (Pg C yr^{-1})[34,40].

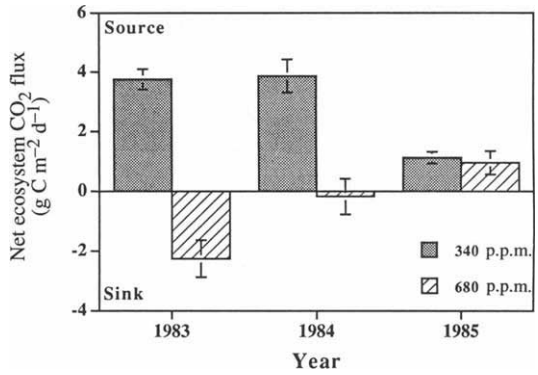

FIG. 1 Seasonal CO_2 flux of tussock tundra (dominated by *Eriophorum vaginatum*) ecosystems exposed to 340 and 680 p.p.m. CO_2 during the 1983–85 growing seasons at Toolik Lake, Alaska. Data are means ±1 standard error; $n = 3$ chambers per treatment.

Recent measurements of CO_2 flux in Arctic ecosystems indicate that tussock and wet sedge tundra are now sources of CO_2 to the atmosphere[34,41,42] possibly due to changes in site water balance[34,40,41,43] following the recently reported increase in northern-latitude surface temperatures[44–48].

Given the huge below-ground carbon stocks in Arctic soils, the release of CO_2 from Arctic ecosystems may exert a positive feedback on atmospheric CO_2 levels and greenhouse warming[41]. Conversely, under conditions of elevated CO_2 and global climate change, northern ecosystems could become a sink for carbon, providing a negative feedback on atmospheric CO_2 levels[34]. The ultimate role of Arctic ecosystems in the global carbon budget largely depends on both the short- and long-term ecosystem response to elevated CO_2 and concomitant climate change.

Higher atmospheric CO_2 has the potential to increase plant growth in a variety of ways, including greater photosynthesis, higher water-use efficiency, depression of respiration, delayed leaf senescence, and relief of nutrient stress via enhanced nutrient-use efficiency, nitrogen fixation and nutrient uptake[3,8,9,16,49]. There is, however, great uncertainty about whether these responses will hold for periods of years in natural

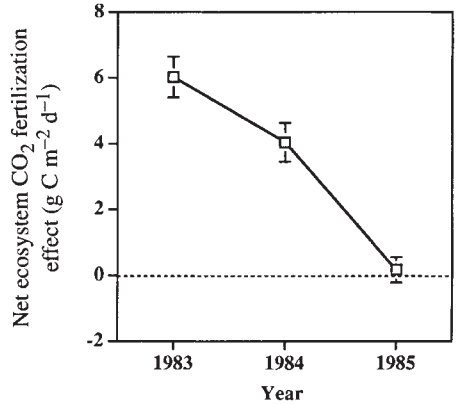

FIG. 2 The CO_2 fertilization effect over three growing seasons at Toolik Lake. Indicated is the absolute stimulation of net ecosystem CO_2 flux by a doubling of atmospheric CO_2 concentration (from 340 to 680 p.p.m.). The CO_2 fertilization effect is calculated as the difference between the flux measured at double and ambient CO_2 levels. Data are means ±1 standard error; $n = 3$ chambers per treatment.